PAPER

Check for updates

Pyrolytic behavior of a zero-valent iron biochar composite and its Cu(II) removal mechanism

Changjiang Yu,[ab] Dashuai Zhang,[a] Xinyu Dong[a] and Qiang Lin (ID) *[ab]

The reduction behavior of Fe^{3+} during the preparation of a zero-valent iron cocoanut biochar (ZBC8-3) by the carbothermic reduction method was analyzed. Fe^{3+} was first converted into Fe_3O_4, which was subsequently decomposed into FeO, and finally reduced to Fe^0. A minor amount of γ-Fe_2O_3 was produced in the process. The isothermal thermodynamic data for the removal of Cu(II) over ZBC8-3 followed a Langmuir model. The Langmuir equation revealed a maximum removal capacity of 169.49 mg g^{-1} at pH = 5 for ZBC8-3. The removal of Cu(II) over ZBC8-3 fitted well to a pseudo-first-order equation, which suggested that the rate limiting step of the process was diffusion. The Cu(II) removal mechanism on ZBC8-3 involved the reduction of Cu(II) by Fe^0 to produce Cu^0 and Cu_2O, while C=C, C–O–, and –O–H formed a complex with Cu(II).

1. Introduction

Owing to its large specific surface area and high reactivity, nanoscale zero-valent Fe (nZVI) has received increasing attention as a removal material for a variety of heavy metals and chlorinated organic contaminants through chemical reduction processes.[1] However, nZVI is extremely unstable and typically suffers from agglomeration and oxidation processes by non-target chemicals during operation. This has hindered significantly the utilization of nZVI for environmental remediation purposes.[2] Up to now, efforts have been focused on increasing the stability and dispersion of nZVI particles. In this sense, a method involving liquid-phase reduction of Fe^{3+} or Fe^{2+} to nZVI and subsequent dispersion of the reduced species on porous materials such as zeolites,[3] attapulgite,[4] graphite,[5] wheat straw,[6] functionalized waste rock wool[7,8] and biochar[9,10] has been widely used. In addition, polyvinyl alcohol (PVA)-alginate-entrapped nanoscale zero-valent iron has been also used to improve the stability of nZVI.[11]

Although these nZVI composites fabricated by liquid-phase reduction have demonstrated good removal capacities, this method requires the utilization of expensive and highly toxic reducing agents such as borohydride. In addition, N_2 protection or vacuum processing is required during the fabrication, and a large amount of toxic by-products are generated. These issues have significantly increased the fabrication costs and the risks of environment pollution.

An alternative approach to produce nZVI for environmental remediation purposes is the carbothermic reduction method. In this method, an Fe-rich precursor is mixed with biomass and subsequently cofired under low-oxygen conditions.[12] However, the reduction behavior of the Fe-rich precursor remains unclear. The main objective of this work is to determine the reduction behavior of the Fe-rich precursor during the preparation of a nZVI-biochar composite. Furthermore, the Cu(II) removal mechanism on the nZVI-biochar composite has not been reported yet. Therefore, our work was also aimed to investigate the mechanism for Cu(II) removal over the nZVI-biochar composite.

2. Materials and methods

2.1 Materials

Sodium alginate was purchased from Shanghai Jingchun Technology Co. Ltd. (Shanghai, China), while $FeCl_3\cdot6H_2O$, $CaCl_2$, and NaOH were purchased from Guangzhou chemical reagent factory (Guangzhou, China). $CuCl_2\cdot2H_2O$, $PbCl_2$, $CoCl_2\cdot6H_2O$, and $NaNO_3$ were purchased from Aladdin Holdings Group, and Cu standard liquid was obtained from Shanghai Fusheng Co. Ltd. (Shanghai, China). All analytical grade chemicals were used without further purification.

2.2 Fabrication of magnetic carbon nanoadsorbents

Cocoanut shell was collected from a suburb (Haikou, China), air-dried at 70 °C and ground (below 0.074 mm sieve). 60.0 g of $FeCl_3\cdot6H_2O$ were dissolved in 500 mL of ethanol and the mixture was mechanically stirred for 1 h. 10.0 g of cocoanut shell powder was then mixed with the as-prepared $FeCl_3$ solution and the suspension was stirred continuously for additional 24 h in order to homogenize Fe^{3+} in the cocoanut shell powders.

[a]Key Laboratory of Water Pollution Treatment & Resource Reuse of Hainan Province, Key Laboratory of Tropical Medicinal Plant Chemistry of Ministry of Education, College of Chemistry and Chemical Engineering, Hainan Normal University, No. 99 Longkunnan Road, Haikou 571158, China. E-mail: linqianggroup@163.com

[b]Faculty of Environmental Science and Engineering, Kunming University of Science and Technology, No. 68 Wenchang Road, Kunming 650500, China
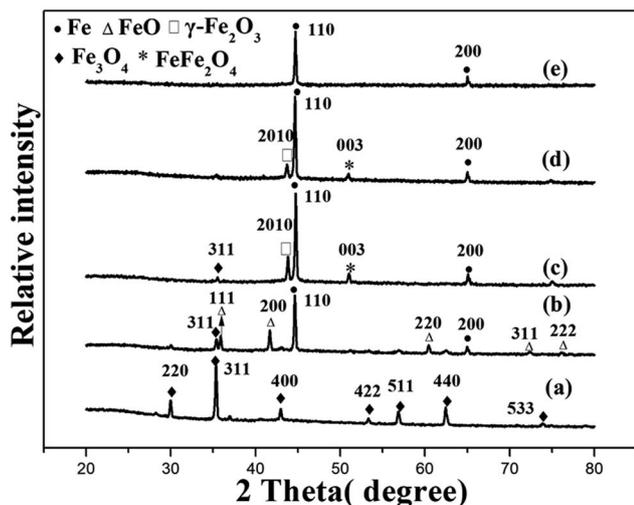
Fig. 1   XRD patterns of ZBC7-1 (a), ZBC7-3 (b), ZBC8-1 (c), ZBC8-2 (d) and ZBC8-3 (e).
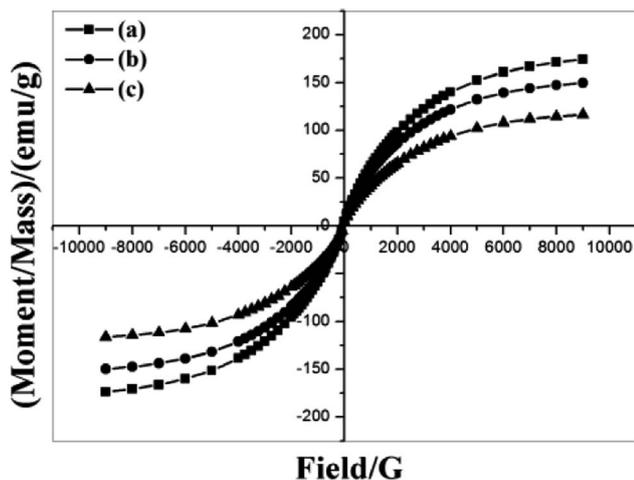

Fig. 2   The magnetization curves of ZBC8-3 (a), ZBC8-2 (b) and ZBC8-1 (c).

The mixture was kept at room temperature for one month. The remaining solids were dried in a convection oven at 120 °C for 10 h and pyrolyzed under nitrogen in a tube furnace to form magnetic carbon nanoadsorbents. The pyrolysis temperature was increased to 200 °C at 5 °C min^{-1} and subsequently increased to 700 or 800 °C at 10 °C min^{-1} and held for 1–3 h. The samples were named as ZBC a–b, where "a" and "b" denote the carbonization temperature and the retention time, respectively.

2.3   Characterization

The Cu(II) concentration was determined by atomic absorption spectrophotometry (AAS, AA-7000, Shimadzu, Japan). The morphology of the samples was investigated by scanning electron microscopy (SEM, JSM-7401F, JEOL, Japan). Surface element analysis was conducted by energy dispersive

spectroscopy (EDS). The structural and compositional characteristics of the materials were investigated by X-ray diffraction (XRD, UItima IV, Rigaku, Japan). X-ray photoelectron spectroscopy (XPS, PHI5000 Versaprobe-II, Ulvac-Phi, Japan) was used to analyze the chemical composition of the magnetic microspheres. The magnetic properties were determined using a magnetic property measurement system (7404, LakeShore, USA). The Fourier transform infrared (FTIR) spectra of the samples were obtained on a Nicolet 6700 infrared spectroscope (Thermo Electro Corp, USA).

2.4   Adsorption kinetic studies

The adsorption experiments on ZBC8-3 were carried out at 25 °C. A Cu(II) stock solution of 100 mg L^{-1} was prepared by dissolving $CuCl_2 \cdot 2H_2O$ in ultra-pure water. The solution was adjusted at pH = 5 using either 0.1 M HNO_3 or 0.1 M NaOH solutions. A certain amount of ZBC8-3 was added to 500 mL of a Cu(II) solution in a beaker and shaken at a constant speed (120 rpm) on a shaking table. 1 mL of the Cu(II) solution was removed at different times (from 10 min to 32 h) and analyzed after dilution.[13] All the results were obtained by taking an average of three specimens. The adsorption capacity of Cu(II) at time t (q_t) was then calculated using eqn (1):

$$q_t = \frac{(C_0 - C_t)V}{m} \tag{1}$$

where C_0 (mg L^{-1}) is the initial Cu(II) concentration, C_t (mg L^{-1}) is the Cu(II) concentration at time t, V is the volume (L) of the Cu(II) solution, and m is the weight (g) of ZBC8-3.

2.5   Adsorption isotherms

0.05 g of ZBC8-3 were added to Cu(II) solutions (200 mL) with different concentrations (50–250 mg L^{-1}) at 25 °C and shaken at a constant speed (120 rpm) for 24 h.[14] Cu(II) was quantified as in the case of the kinetic studies. All the results were obtained by taking an average of three specimens. The equilibrium adsorption capacity of Cu(II) (q_e) was calculated using eqn (2):

$$q_e = \frac{(C_0 - C_e)V}{m} \tag{2}$$

where C_0 (mg L^{-1}) and C_e are the initial and equilibrium concentrations of Cu(II), respectively, V is the volume (L) of the Cu(II) solution, and m is the weight (g) of ZBC8-3.

2.6   Influence of other ions on the Cu(II) removal ability of ZBC8-3

The hygienic standard for drinking water in China requires the Cu(II) concentration in drinking water to be less than 1 mg L^{-1}, while nitrate concentration must be lower than 10 mg L^{-1}. In this study, a Cu(II) solution of 10 mg L^{-1} was selected as the simulated pollution source, while a $NaNO_3$ solution of 10 mg L^{-1} was selected as a background electrolyte. To be specific, the Cu(II) solution of 10 mg L^{-1} fabricated by dissolving $CuCl_2$ in ultrapure water was marked as sample 1. Both Cu(II)
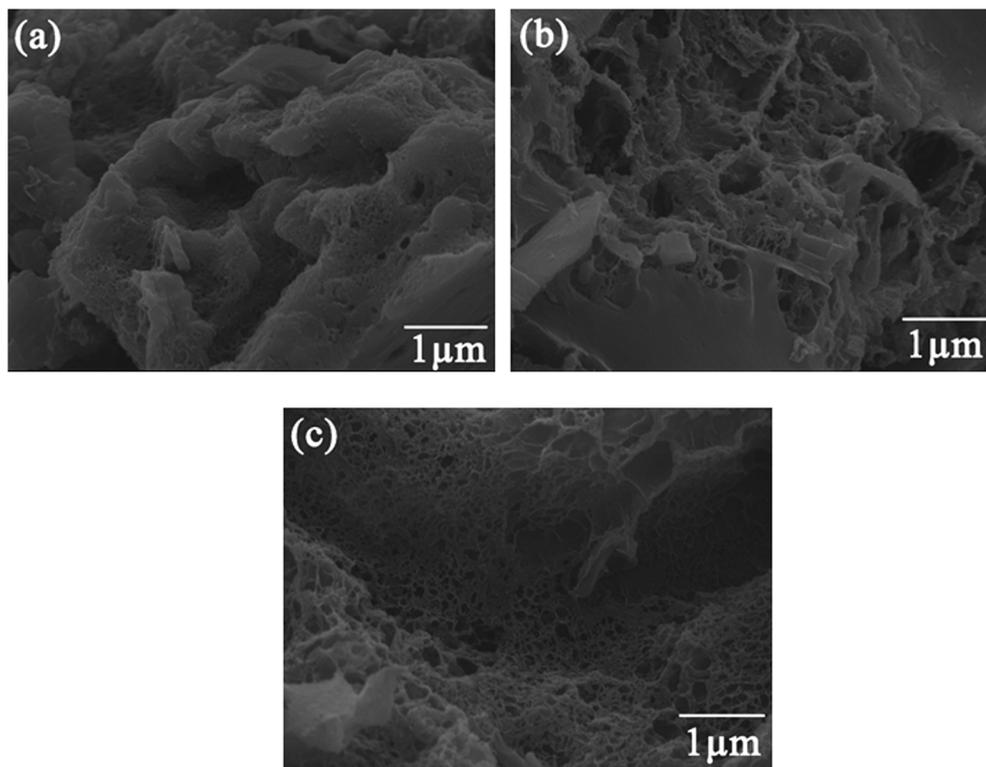
Fig. 3 SEM images of the surface of ZBC8-1 (a), ZBC8-2 (b) and ZBC8-3 (c).

and $NaNO_3$ 10 mg L^{-1} solutions were marked as samples 2. In addition, Pb(II)/Cu(II), Co(II)/Cu(II), and Pb(II)/Co(II)/Cu(II) mixtures were prepared by adding $PbCl_2$ and $CoCl_2$ to samples 2, respectively, and were marked as samples 3, 4, and 5. Moreover, 0.1 g of ZBC8-3 were added respectively to samples 1–5 and shaken at a constant speed (120 rpm) at 25 °C for 24 h. After shaking, ZBC8-3 was filtered and the concentrations of Cu(II) in the filtered solutions were determined by AAS. All the results were obtained by taking an average of three specimens.

Fig. 4 N_2 adsorption–desorption isotherms and pore size distributions of ZBC8-3.

3. Results and discussion

3.1 Characterization of materials

3.1.1 Impact of the pyrolysis conditions on the iron ion reduction process.
Fig. 1(a) shows the XRD pattern of ZBC7-1. The characteristic diffraction peaks were consistent with those of the normal card (JCPDS no. 65-3107) of Fe_3O_4.[15] Thus, the 2θ diffraction peaks at 30.1, 35.5, 43.1, 53.5, 57.0, 62.6, and 74.0° corresponded to the crystal planes (220), (311), (400), (422), (511), (440), and (533) of Fe_3O_4, respectively. Fig. 1(b) shows the XRD pattern of ZBC7-3. The characteristic diffraction peaks revealed the presence of Fe^0 (JCPDS no. 06-0696),[16] FeO (JCPDS no. 06-0615),[17] and Fe_3O_4 (JCPDS no. 65-3107).[15] 2θ diffraction peaks at 44.67 and 65.02° corresponded to the crystal planes (110) and (200) of Fe^0 respectively, while those at 36.04, 41.92, 60.76, 72.73, and 76.58° corresponded to crystal planes (111), (200), (220), (311), and (222) of FeO respectively. The peak at 35.5° corresponded to the crystal plane (311) of Fe_3O_4. Fig. 1(c) and (d) show the XRD patterns of ZBC8-1 and ZBC8-2, respectively. An increase in both the pyrolysis temperature and the retention time resulted in most Fe^{3+} being transformed to Fe^0, and the onset of some diffraction peaks of γ-Fe_2O_3 (JCPDS no. 40-1139)[18] and $FeFe_2O_4$ (JCPDS no. 28-0491).[19] As shown in the XRD pattern of ZBC8-3 (Fig. 1(e)), most of Fe^{3+} was reduced to Fe^0.

3.1.2 Magnetic properties.
The hysteresis loops of ZBC8-3 (a), ZBC8-2 (b) and ZBC8-1 (c) are shown in Fig. 2. There were no remanence or coercivity, which indicated that the composites exhibited typical superparamagnetic behavior.[20] The
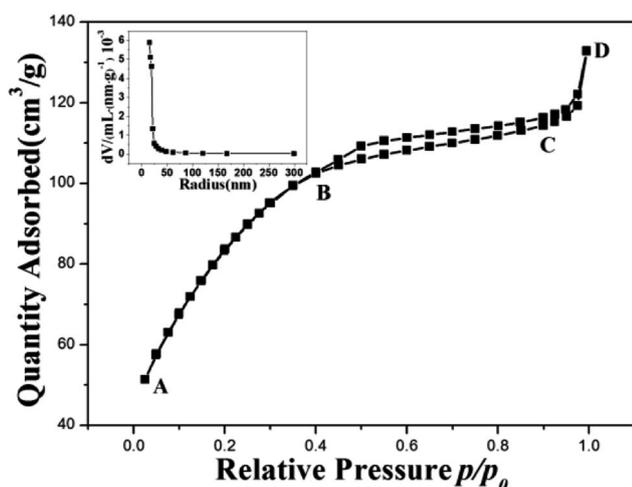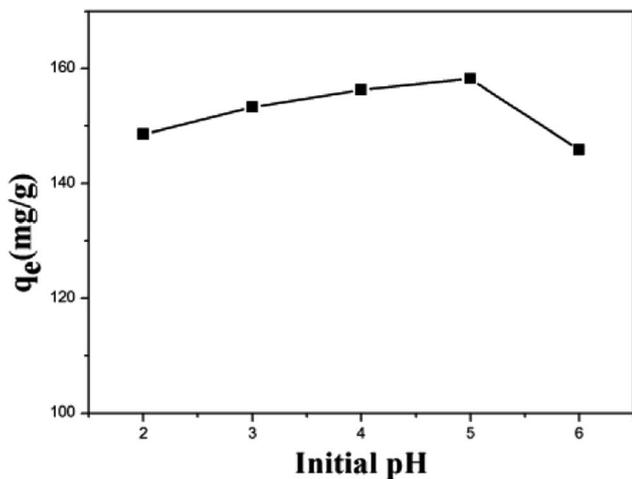
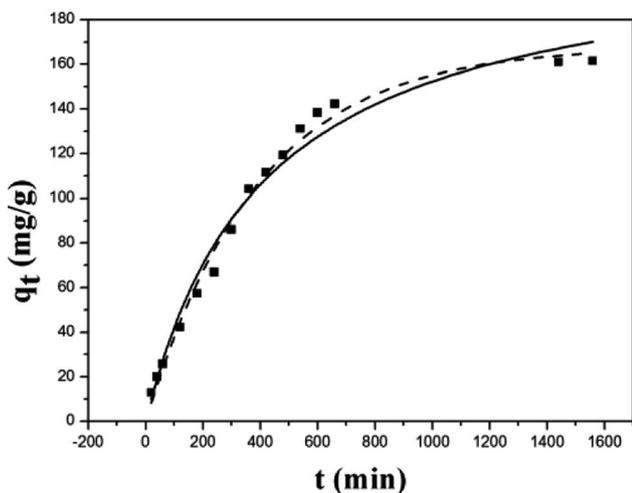**Fig. 5** Effect of the pH on the removal of Cu(II) on ZBC8-3.

Fig. 6 Kinetic adsorption plots of the removal of Cu(II) on ZBC8-3.

maximum saturation magnetizations of ZBC8-3, ZBC8-2, and ZBC8-1 were 170.04, 149.77, and 116.29 emu g^{-1}, respectively. An increase in the retention time might have favored the formation of Fe^0.

3.1.3 SEM analysis. The SEM images of the ZBC8-1 (a), ZBC8-2 (b), and ZBC8-3 (c) samples are shown in Fig. 3. As shown in these pictures, the nZVI-biochar composite underwent a rapid pore development at high retention time. Magnetic carbon nanoparticles were observed on the surface of the nZVI-biochar composite.

3.1.4 N$_2$ adsorption–desorption isotherms and pore size distributions of ZBC8-3. The N$_2$ adsorption–desorption

isotherm and pore size distribution of ZBC8-3 are shown in Fig. 4. N$_2$ adsorbed on ZBC8-3 first forming a monomolecular adsorption layer, which corresponded to the section AB.[21] Capillary condensation started in section BC, which was in the middle of the curve. At this stage, amount of gas adsorbed changed slowly with the relative pressure of N$_2$, revealing a relatively wide ZBC8-3 pore diameter distribution.[21] In the section CD, the gas adsorption curve increased rapidly, and there was no sign of saturated adsorption even at pressures close to the saturated vapor pressure. This result revealed the presence of a certain amount of large pores in the sample with volumetric filling in large pores taking place by capillary condensation.[22] The specific surface area of ZBC8-3 was 310.82 $m^2 g^{-1}$. According to the pore diameter distribution of ZBC8-3, most of the pores showed a radius within 15–25 nm.

3.2 Effect of the pH on the removal of Cu(II)

The Cu(II) removal experiments of ZBC7-1, ZBC7-3, ZBC8-1, ZBC8-2, and ZBC8-3 were carried out with a Cu(II) solution of 20 mg L^{-1} under constant shaking (120 rpm) for 24 h at pH = 5. The results showed that the removal capacity of ZBC7-1, ZBC7-3, ZBC8-1, ZBC8-2, and ZBC8-3 were 10.28, 29.15, 50.54, 61.86, and 73.50 mg g^{-1}, respectively. An increase in the carbonization temperature and the retention time might have favored the formation of Fe^0. Therefore, ZBC8-3 was selected as the raw material for subsequent experiments. The effect of the pH on the removal capacity of ZBC8-3 was investigated. Adsorption experiments were carried with a Cu(II) solution of 90 mg L^{-1} over a pH range of 2–6, since Cu(II) precipitate above a pH of 6.[23] All the results were obtained by taking an average of three specimens.

The removal capacity of ZBC8-3 increased quickly with the pH (Fig. 5). This can be explained as follows. At lower pH, a higher number of very mobile protons (H^+) compete with Cu(II) ions for the active sites on ZBC8-3. Upon increasing the pH, the concentration of H^+ ions decreased, resulting in more Cu(II) being replaced.[24] In addition, the Cu(II) removal capacity of ZBC8-3 decreased significantly at a pH of = 6, which may result from Fe^{3+}/Fe^{2+} depositions easily generated at high pH covering the surface of ZBC8-3. These deposits prevented the diffusion of Cu(II) into ZBC8-3. Therefore, pH = 5 was chosen as the optimum experimental conditions.[25]

3.3 Kinetics adsorption experiments

The kinetics of the Cu(II) removal on ZBC8-3 were investigated by using dynamic data. Pseudo-first-order and pseudo-second-order kinetic models were applied to fit the data, as described in eqn (3) and (4).[26] The result for non-linear curve fitting to the dynamic data is shown in Fig. 6:

Table 1 Kinetics parameter coefficients for Cu(II) removal on ZBC8-3

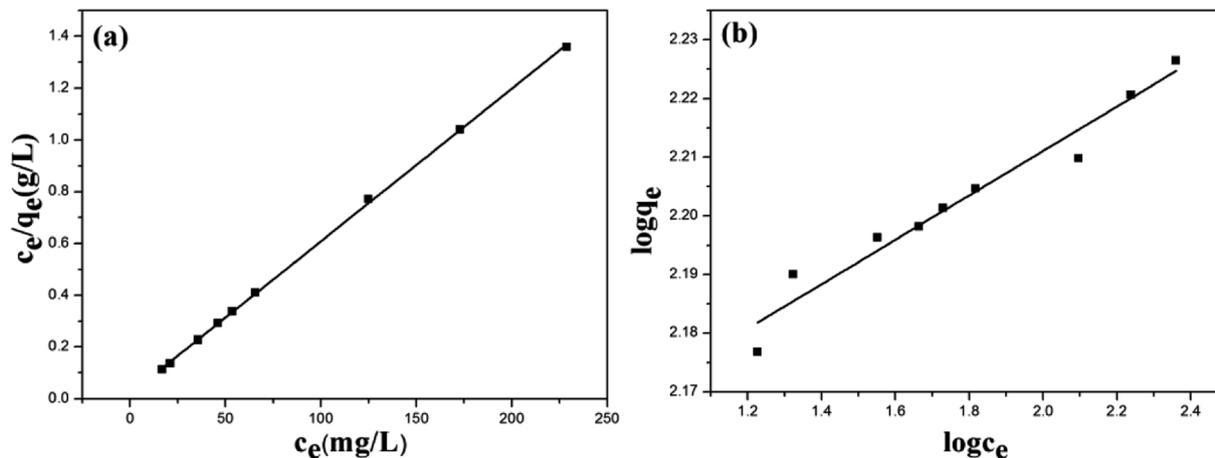|	Pseudo-first-order model			Pseudo-second-order model		
Sample	$q_{e,cal}$ (mg g^{-1})	k_1 (10^{-3} min^{-1})	R^2	$q_{e,cal}$ (mg g^{-1})	k_2 (10^{-4} g mg^{-1} min^{-1})	R^2
ZBC8-3	168.11	2.57	0.9908	214.67	0.1139	0.9785

Fig. 7 Adsorption isotherms of Langmuir (a) and Freundlich (b) equations for the removal of Cu(II) on ZBC8-3.

Table 2 Isotherm parameters for the removal of Cu(II) on ZBC8-3

	Langmuir			Freundlich		
Sample	q_m (mg g^{-1})	K_L (L mg^{-1})	R^2	$1/n$	K_F (mg g^{-1})	R^2
ZBC8-3	169.49	0.3181	0.9997	0.0378	136.58	0.9510

$$\log(q_e - q_t) = \log q_e - \left(\frac{k_1}{2.303}\right)t \quad (3)$$

$$\frac{t}{q_e} = \frac{1}{k_2 q_e^2} + \frac{t}{q_e} \quad (4)$$

where q_t and q_e are the amounts of Cu(II) removed per unit mass of ZBC8-3 in mg g^{-1} at an arbitrary contact time t (s) and at equilibrium stage. k_1 and k_2 are the pseudo-first-order and pseudo-second-order kinetic constants expressed in min^{-1} and g mg^{-1} min^{-1}, respectively.

As shown in Fig. 6, the removal of Cu(II) on ZBC8-3 was fast within the first 6 h, and the rate decreased thereafter and stabilized within 24 h. The relatively fast removal rate within the first 6 h was mainly attributed to an oxidation–reduction reaction of Fe^0 on the outer layer of ZBC8-3. Some deposits were formed by redox reaction of Fe^0 and Cu(II), blocking the pore

structure of the ZBC8-3 to some extent. As a result, diffusion of Cu(II) to the inside of the ZBC8-3 was hindered in the consequent reaction.

The kinetic model parameters as well as the correlation coefficient (R^2) for ZBC8-3 are included in Table 1.

The pseudo-first-order equation described the Cu(II) removal behavior on ZBC8-3. The correlation coefficient (0.9908) for ZBC8-3 was higher than that of the pseudo-second-order equation (0.9785), indicating that the rate limiting step was diffusion.[27] Thus, the surface of ZBC8-3 was covered by deposits, which blocked the porous structure of ZBC8-3. Cu(II) ions gradually diffused to the interior of ZBC8-3, and the overall process required more time to complete.

3.4 Isothermal adsorption experiments

The removal isotherms were fitted using the Langmuir and Freundlich isotherm models. The Langmuir isotherm model is described by eqn (5):[28]

$$\frac{c_e}{q_e} = \frac{1}{K_L q_m} + \frac{c_e}{q_m} \quad (5)$$

where, c_e (mg L^{-1}) is the concentration of Cu(II) ions at equilibrium, q_m (mg g^{-1}) is the Langmuir adsorption maximum, K_L is the coefficient of distribution for the removal of Cu(II), and q_e

Table 3 Comparison of the adsorption potential of various adsorbents for copper ion removal from water

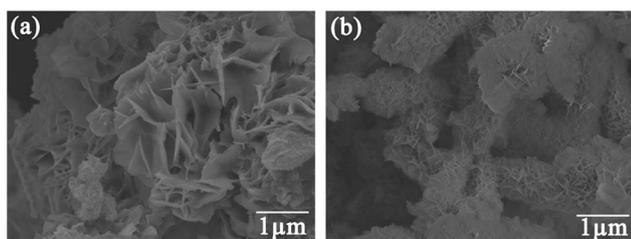| Adsorbents	pH	Concentration range (mg L^{-1})	Q_{max} (mg g^{-1})	Ref.
Functionalized magnetic nanoparticles	5	10–100	34.08	31
Mg–Al-D$_2$EHPA	5	100	68.66	32
M-HAP/agar composite beads	5	10–200	71.6	33
Carbon aerogels	—	0–400	86.27	22
Sugarcane bagasse trimellitate	5.5	60	67.84	34
Bifunctional ordered mesoporous silica	5	10–50	90.61	35
Ph-PAni nanofibers	5.3	6.4–64	5.29	36
Magnetic nanoscale zerovalent iron assisted biochar	6	—	30.37	37
Chitosan enwrapping Fe$_3$O$_4$ and graphene oxide	6	500	132	38
ZBC8-3	5	50–250	169.49	This study
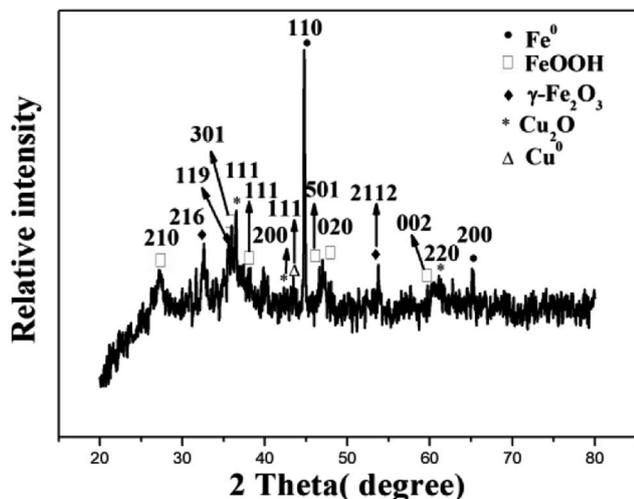
Fig. 8 XRD pattern of ZBC8-3 after Cu(ɪɪ) removal.

Fig. 9 SEM images of the surface of ZBC8-3 after Cu(ɪɪ) removal.

is the amount of Cu(ɪɪ) ions removed per unit mass of ZBC8-3 in mg g^{-1} at equilibrium stage.

The Freundlich isotherm model is described by eqn (6):[29]

$$\log q_e = \log K_F + \frac{1}{n} \log C_e \qquad (6)$$

K_F is the coefficient of distribution for the adsorption process.

The Langmuir and Freundlich isotherms of ZBC8-3 are shown in Fig. 7. The results showed that the Cu(ɪɪ) ion removal

Fig. 11 FTIR pattern of ZBC8-3 before and after being treated with Cu(ɪɪ).

capacity increased rapidly at low concentrations of Cu(ɪɪ) and gradually reached its maximum by increasing the Cu(ɪɪ) ion concentration.

The isotherms model parameter and the correlation coefficient (R^2) for ZBC8-3 are summarized in Table 2.

As shown in Table 2, the correlation coefficient of the Langmuir model adsorption isotherm plots was high (0.9997) for the ZBC8-3. The high R^2 suggested that the Langmuir model fitted the adsorption data well. The homogeneous nature of the active sites on the adsorbents might have favored a monolayer removal behavior of Cu(ɪɪ) ions on ZBC8-3.[30]

3.5 Comparison with other adsorbents

The removal capacity (q_m) for Cu(ɪɪ) on ZBC8-3 obtained herein was comparable with those reported in the literature for other adsorbents (Table 3). ZBC8-3 showed promising results for the removal of Cu(ɪɪ) from aqueous solutions (*i.e.*, a relatively high removal capacity).
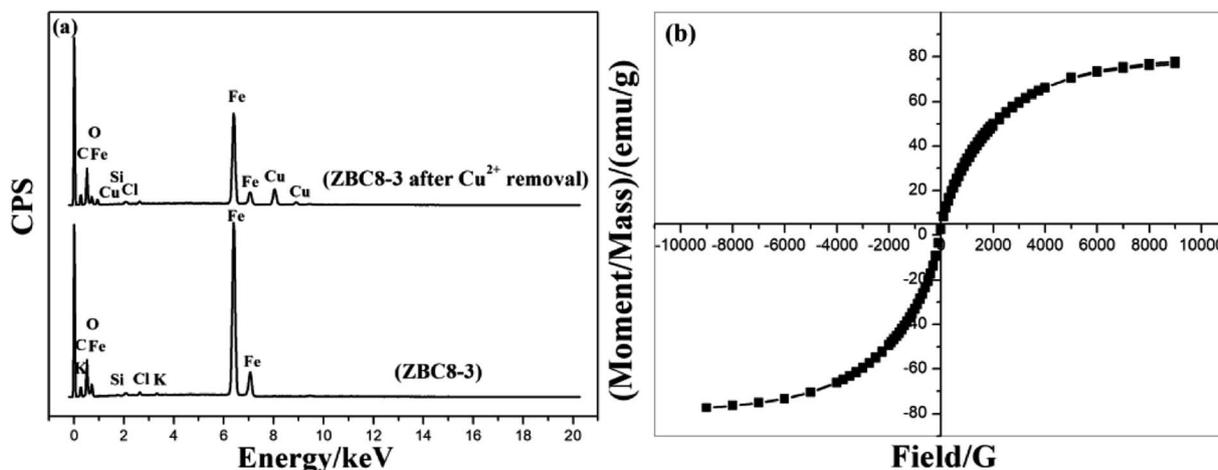

Fig. 10 EDS pattern of ZBC8-3 before and after Cu(ɪɪ) removal (a) and the magnetization curve of ZBC8-3 after Cu(ɪɪ) removal (b).
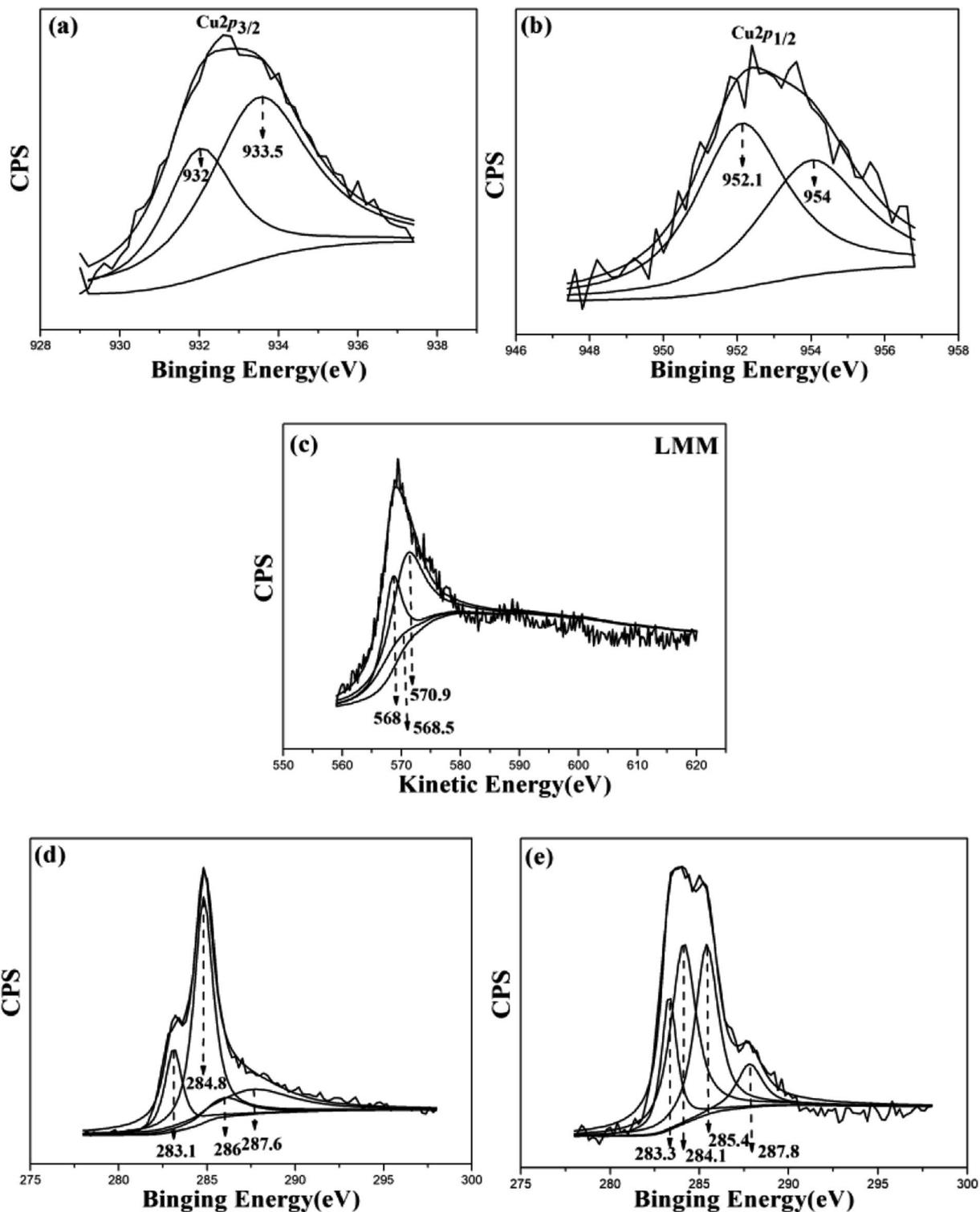
Fig. 12   Cu2p$_{3/2}$ for ZBC8-3 after Cu(II) removal (a), Cu 2p$_{1/2}$ for ZBC8-3 after Cu(II) removal (b), Cu LMM for ZBC8-3 after Cu(II) removal (c), C 1s for ZBC8-3 before (d) and after (e) Cu(II) removal.

3.6   Adsorption mechanism

Fig. 8 shows the XRD pattern of ZBC8-3 after reaction with Cu(II). The characteristic diffraction peaks revealed the presence of Cu$_2$O (JCPDS no. 05-0667),[39] γ-Fe$_2$O$_3$ (JCPDS no. 25-1402)[40], FeOOH (JCPDS no. 44-1415),[41] Fe^0 (JCPDS no. 06-0696)[41] and

Cu^0 (JCPDS no. 04-0836).[42] The 2θ diffraction peaks at 36.42, 42.30, and 61.34° corresponded to the crystal planes (111), (200), and (220) of Cu$_2$O, respectively. The peaks at 32.17, 35.68, and 50.08° corresponded to the crystal planes (216), (119), and (2112) of γ-Fe$_2$O$_3$, respectively. The peaks at 27.04, 36.29, 38.07,

46.78, 46.91, and 60.26° were ascribed to the crystal planes (210), (301), (111), (501), (020), and (002) of FeOOH. In addition, the XRD pattern indicated the presence of Fe^0 (2θ = 44.67 and 65.02°) and Cu^0 (2θ = 43.30°). Therefore, from the results of Fig. 8, most of Cu(II) was reduced to Cu^0 and Cu_2O, while most of nZVI was converted to FeOOH and γ-Fe_2O_3. In addition, a fraction of nZVI did not react with Cu(II).

Fig. 9 shows the SEM patterns of ZBC8-3 after reaction with Cu(II). ZBC8-3 was covered by the reaction products (e.g., Cu_2O, Cu^0, FeOOH, and γ-Fe_2O_3) on its surface. The original porous structure of ZBC8-3 was therefore blocked.

Fig. 10(a) shows the EDS patterns of ZBC8-3 before and after reaction with Cu(II). The results revealed that the amount of Fe on ZBC8-3 decreased after reaction with Cu(II) from 82.87 to 56.74 wt%. The amount of Cu on the surface of ZBC8-3 after reaction with Cu(II) was 19.95 wt%. As shown in Fig. 10(b), the maximum saturation magnetization of ZBC8-3 after reaction with Cu(II) was 77.6 emu g^{-1}. Thus, the solid can be separated readily by using a magnet.

FTIR was used to study the molecular interactions and analyze the functional groups of ZBC8-3 before and after the Cu(II) removal process. As shown in Fig. 11, ZBC8-3 revealed a stretching vibration peak of O–H at 3432.58 cm^{-1},[30] a stretching vibration peak of C=O at 1627.02 cm^{-1},[43] stretching vibration peak of aromatic ring at 1549.64, 1531.92, and 1513.01 cm^{-1},[44] stretching vibration peaks of C–O–C and Si–O at 1088.18 cm^{-1},[45] and a bending vibration peak of Fe–O at 477.01 cm^{-1}.[46] The adsorption peak was characteristic of the Fe–O bond, possibly because part of Fe^0 was oxidized during the grinding process. The FTIR spectra of ZBC8-3 after Cu(II) removal revealed that some adsorption peaks were slightly shifted. The stretching vibration peaks of the aromatic ring, C–O–C, and Si–O shifted to lower wavenumber, which might result from those functional groups being complexed with Cu(II). The increased ionic volume weakened the stretching and bending vibrations of the functional groups and caused the downfield shift.[47] The O–H peak after Cu(II) removal was observed at longer wavenumbers than before the removal process. This shifting to higher wavenumbers may be attributed to an inductive effect.[48] The wavelength of the C=O peak hardly changed after Cu(II) removal. In addition, several new peaks ascribed to FeOOH appeared for ZBC8-3 after Cu(II) removal. (i.e., a bending vibration peak of Fe–O at 417.39 cm^{-1}[46] and stretching vibration peaks of O–H at 3362.27 and 3313.65 cm^{-1})[49].

The XPS analysis of Cu in ZBC8-3 after reaction with Cu(II) is shown in Fig. 12(a) and (b). Each adsorption peak of Cu $2p_{3/2}$ and Cu $2p_{1/2}$ were deconvoluted into 2 peaks. The peaks at 932 and 952.1 eV could be ascribed to Cu_2O and Cu^0 species, respectively, while, the adsorption peaks at 933.5 and 954 eV could be ascribed to Cu(II) species. Auger electron spectroscopy was used to study Cu more in detail (Fig. 12(c)). With reference to the standard data, the adsorption peaks at 568, 568.5, and 570.9 eV could be ascribed to Cu^0, Cu(II), and Cu_2O species, respectively. The XPS analysis for C in ZBC8-3 is shown in Fig. 12(d). The adsorption peak at 283.1 eV could be ascribed to Si–C bond,[50] the adsorption peak at 284.8 eV could be ascribed to C–C or C=C bonds,[44,51] the adsorption peak at 286 eV can be
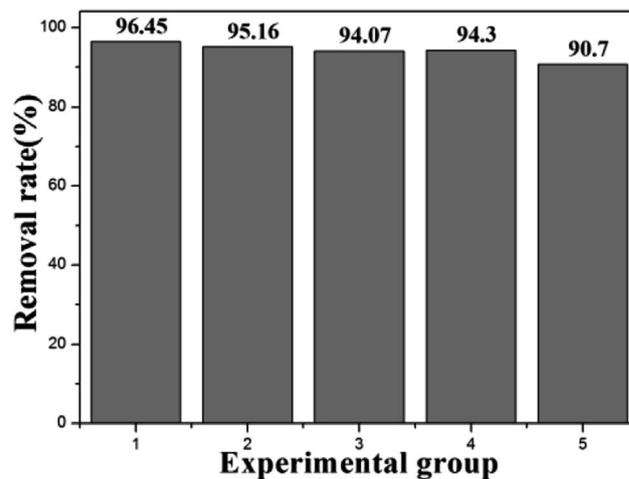

Fig. 13 The effect of other ions on ZBC8-3 removal of Cu(II).

produced by C–O bond, and the peak at 287.6 eV could be attributed to C=O bonds.[44,51] The XPS analysis for C in ZBC8-3 after reaction with Cu(II) is shown in Fig. 12(e). The binding energy of Si–C and C=O changed slightly before and after Cu(II) removal, which indicated that Si–C and C=O may not involve the removal of Cu(II). The binding energy of C=C and C–O decreased significantly compared to those before the removal of Cu(II), which indicated that C=C, C–O, and Cu(II) species could have formed a coordination compound. Thus, the binding energy of the functional groups was reduced owing to changes in the electronic densities of the groups in relation with their local environment.[52]

3.7 The effect of other ions on the removal of Cu(II) on ZBC8-3

Fig. 13 shows the effect of other ions on the removal of Cu(II) over ZBC8-3. The Cu(II) removal rate of sample 2 was slightly lower than that of sample 1. Thus, nitrate showed a certain influence on the removal of Cu(II). The Cu(II) removal rates of samples 3 and 4 were lower than that of sample 2. Pb(II) and Co(II) ions showed a comparatively large influence on the removal of Cu(II). The Cu(II) removal rate of sample 5 decreased significantly, while the Cu(II) concentrations of samples 1, 2, 3, 4 and 5 were 0.35, 0.48, 0.59, 0.57 and 0.93 mg L^{-1} after Cu(II) removal, respectively. Since the standard electrode potential of $E^{\ominus}_{Cu^{2+}/Cu}$ (0.342 V) is higher than that of $E^{\ominus}_{Pb^{2+}/Pb}$ (−0.126 V) and $E^{\ominus}_{Co^{2+}/Co}$ (−0.28 V), Cu(II) ions are more easily reduced. Since the hygienic standard for drinking water in china requires that Cu(II) concentrations in drinking below 1 mg L^{-1}, ZBC8-3 can be used to remove Cu(II) ions from wastewater.

4. Conclusions

A nZVI biochar composite derived from cocoanut shell was fabricated by a calcination method by using $FeCl_3$ as the iron precursor. The maximum saturation magnetization of ZBC8-3 before and after Cu(II) removal were 170.04 and 77.6 emu g^{-1}, respectively, allowing easy separation of the solid after Cu(II) removal by using a magnet. The Cu(II) removal capacity of ZBC8-

3 was as high as 169.49 mg g^{-1} because of its higher content of nZVI. Thus, this material can be used to remove Cu(II) ions from wastewater.

Conflicts of interest

There are no conflicts.

Acknowledgements

References

1 L. Qian, W. Zhang, J. Yan, L. Han, Y. Chen, D. Ouyang and M. Chen, *Environ. Pollut.*, 2017, **223**, 153–160.

2 X. Jiang, Z. Ouyang, Z. Zhang, C. Yang, X. Li, Z. Dang and P. Wu, *Colloids Surf., A*, 2018, **547**, 64–72.

3 Z. Li, L. Wang, J. Meng, X. Liu, J. Xu, F. Wang and P. Brookes, *J. Hazard. Mater.*, 2018, **344**, 1–11.

4 L. Dong, L. Lin, Q. Li, Z. Huang, X. Tang, M. Wu, C. Li, X. Cao and M. Scholz, *J. Environ. Manage.*, 2018, **213**, 151–158.

5 C. Xu, W. Yang, W. Liu, H. Sun, C. Jiao and A.-j. Lin, *J. Environ. Sci.*, 2017, DOI: 10.1016/j.jes.2017.11.003.

6 Y. Shao, P. Zhao, Q. Yue, Y. Wu, B. Gao and W. Kong, *Ecotoxicol. Environ. Saf.*, 2018, **158**, 100–107.

7 L. Zhou, R. Li, G. Zhang, D. Wang, D. Cai and Z. Wu, *Chem. Eng. J.*, 2018, **339**, 85–96.

8 D.-l. Kong, G.-p. Lu, M.-s. Wu, Z.-f. Shi and Q. Lin, *ACS Sustainable Chem. Eng.*, 2017, **5**, 3465–3470.

9 W. Shi and X. Song, *Advances in Energy and Environmental Materials*, 2018, pp. 885–895, DOI: 10.1007/978-981-13-0158-2_89.

10 C.-M. Liu, Z.-H. Diao, W.-Y. Huo, L.-J. Kong and J.-J. Du, *Environ. Pollut.*, 2018, **239**, 698–705.

11 Y. Sun, C. Lei, E. Khan, S. Chen, D. Tsang, Y. Ok, D. Lin, Y. Feng and X. Li, *Sci. Total Environ.*, 2018, **615**, 498–507.

12 D. W. Cho, G. Kwon, Y. S. Ok, E. E. Kwon and H. Song, *ACS Appl. Mater. Interfaces*, 2017, **9**, 13142–13150.

13 C. Yu, M. Wang, X. Dong, Z. Shi, X. Zhang and Q. Lin, *RSC Adv.*, 2017, 7, 53135–53144.

14 Y. Guo, W. Tang, J. Wu, Z. Huang and J. Dai, *J. Environ. Sci.*, 2014, **26**, 2123–2130.

15 L. Yan, S. Li, H. Yu, R. Shan, B. Du and T. Liu, *Powder Technol.*, 2016, **301**, 632–640.

16 T. F. Marinca, H. F. Chicinaș, B. V. Neamțu, O. Isnard and I. Chicinaș, *J. Alloys Compd.*, 2015, **652**, 313–321.

17 Y. Yin, M. Zeng, J. Liu, W. Tang, H. Dong, R. Xia and R. Yu, *Sci. Rep.*, 2016, **6**, 25075.

18 S. Zhang, L. Tao, M. Jiang, G. Gou and Z. Zhou, *Mater. Lett.*, 2015, **157**, 281–284.

19 Y. Tang, H. Zhang, J. Li, G. Hou, H. Cao, L. Wu, G. Zheng and Q. Wu, *J. Alloys Compd.*, 2017, **719**, 203–209.

20 C. Yu, J. Geng, Y. Zhuang, J. Zhao, L. Chu, X. Luo, Y. Zhao and Y. Guo, *Carbohydr. Polym.*, 2016, **152**, 327–336.

21 Z. Wang, Y. Cheng, K. Zhang, C. Hao, L. Wang, W. Li and B. Hu, *Fuel*, 2018, **232**, 495–505.

22 L. I. U. Hong-Bo, L. I. Jin and Z. Lei, *J. Inorg. Mater.*, 2017, **32**, 1159.

23 M. Li, Q. Liu, L. Guo, Y. Zhang, Z. Lou, Y. Wang and G. Qian, *Bioresour. Technol.*, 2013, **141**, 83–88.

24 N. Jiang, Y. Xu, Y. Dai, W. Luo and L. Dai, *J. Hazard. Mater.*, 2012, **215–216**, 17–24.

25 P. Regmi, J. L. Garcia Moscoso, S. Kumar, X. Cao, J. Mao and G. Schafran, *J. Environ. Manage.*, 2012, **109**, 61–69.

26 H. Tavakoli, H. Sepehrian and R. Cheraghali, *J. Taiwan Inst. Chem. Eng.*, 2013, **44**, 343–348.

27 M. Zhang, B. Gao, S. Varnoosfaderani, A. Hebard, Y. Yao and M. Inyang, *Bioresour. Technol.*, 2013, **130**, 457–462.

28 Y. Li, Q. Du, T. Liu, J. Sun, Y. Wang, S. Wu, Z. Wang, Y. Xia and L. Xia, *Carbohydr. Polym.*, 2013, **95**, 501–507.

29 L. Liu, Y. Wan, Y. Xie, R. Zhai, B. Zhang and J. Liu, *Chem. Eng. J.*, 2012, **187**, 210–216.

30 B. Wang, C. Li and H. Liang, *Bioresour. Technol.*, 2013, **146**, 803–806.

31 M. O. Ojemaye, O. O. Okoh and A. I. Okoh, *Sep. Purif. Technol.*, 2017, **183**, 204–215.

32 N. Rouahna, D. Barkat, A. Ouakouak and E. Srasra, *J. Environ. Chem. Eng.*, 2018, DOI: 10.1016/j.jece.2018.01.036.

33 Q. Zhang, S. Dan and K. Du, *Ind. Eng. Chem. Res.*, 2017, **56**, 8705–8712.

34 A. L. P. Xavier, O. F. H. Adarme, L. M. Furtado, G. M. D. Ferreira, L. H. M. da Silva, L. F. Gil and L. V. A. Gurgel, *J. Colloid Interface Sci.*, 2018, **516**, 431–445.

35 S. J. Mousavi, M. Parvini and M. Ghorbani, *J. Taiwan Inst. Chem. Eng.*, 2018, **84**, 123–141.

36 H. J. Kim, S. Im, J. C. Kim, W. G. Hong, K. Shin, H. Y. Jeong and Y. J. Hong, *ACS Sustainable Chem. Eng.*, 2017, **5**, 6654–6664.

37 S. Zhu, S.-H. Ho, X. Huang, D. Wang, F. Yang, L. Wang, C. Wang, X. Cao and F. Ma, *ACS Sustainable Chem. Eng.*, 2017, **5**, 9673–9682.

38 D. Kong, N. Wang, N. Qiao, Q. Wang, Z. Wang, Z. Zhou and Z. Ren, *ACS Sustainable Chem. Eng.*, 2017, **5**, 7401–7409.

39 C. Liu, Y. H. Chang, J. Chen and S. P. Feng, *ACS Appl. Mater. Interfaces*, 2017, **9**, 39027–39033.

40 X. Liu, W. Si, J. Zhang, X. Sun, J. Deng, S. Baunack, S. Oswald, L. Liu, C. Yan and O. G. Schmidt, *Sci. Rep.*, 2014, **4**, 7452.

41 P.-R. Liu, Z.-Y. Yang, Y. Hong and Y.-L. Hou, *Algal Res.*, 2018, **31**, 173–182.

42 Z. Su, L. Tan, R. Yang, Y. Zhang, J. Tao, N. Zhang and F. Wen, *Chem. Phys. Lett.*, 2018, **695**, 153–157.

43 A. F. Hassan, A. M. Abdel-Mohsen and H. Elhadidy, *Int. J. Biol. Macromol.*, 2014, **68**, 125–130.

44 Q. Fang, B. Chen, Y. Lin and Y. Guan, *Environ. Sci. Technol.*, 2014, **48**, 279–288.

45 B. Zhou, Z. Wang, D. Shen, F. Shen, C. Wu and R. Xiao, *Ecol. Eng.*, 2017, **98**, 189–195.

46 X. Wei, Q. Liu, H. Zhang, J. Liu, R. Chen, R. Li, Z. Li, P. Liu and J. Wang, *J. Colloid Interface Sci.*, 2018, **511**, 1–11.

47 G. R. Mahdavinia, S. Mousanezhad, H. Hosseinzadeh, F. Darvishi and M. Sabzi, *Carbohydr. Polym.*, 2016, **147**, 379–391.

48 Y. T. Zhou, C. Branford-White, H. L. Nie and L. M. Zhu, *Colloids Surf., B*, 2009, **74**, 244–252.

49 L. Kuang, Y. Liu, D. Fu and Y. Zhao, *J. Colloid Interface Sci.*, 2017, **490**, 259–269.

50 Q. Zhao, Y. Huang and X. Hu, *Electrochem. Commun.*, 2016, **70**, 8–12.

51 J. M. Lázaro Martínez, E. Rodríguez-Castellón, R. M. T. Sánchez, L. R. Denaday, G. Y. Buldain and V. Campo Dall' Orto, *J. Mol. Catal. A: Chem.*, 2011, **339**, 43–51.

52 C. Bertagnolli, A. Uhart, J. C. Dupin, M. G. da Silva, E. Guibal and J. Desbrieres, *Bioresour. Technol.*, 2014, **164**, 264–269.